

Faculteit Industriële
Ingenieurswetenschappen

master in de industriële wetenschappen: energie

Masterthesis

Optimization of thin film chalcogenide solar cell baseline process

Nick Keppens

Scriptie ingediend tot het behalen van de graad van master in de industriële wetenschappen: energie

PROMOTOR :

Prof. dr. Bart VERMANG

PROMOTOR :

prof. dr. Guy BRAMMERTZ

Gezamenlijke opleiding UHasselt en KU Leuven



Universiteit Hasselt | Campus Diepenbeek | Faculteit Industriële Ingenieurswetenschappen | Agoralaan Gebouw H - Gebouw B | BE 3590 Diepenbeek

Universiteit Hasselt | Campus Diepenbeek | Agoralaan Gebouw D | BE 3590 Diepenbeek
Universiteit Hasselt | Campus Hasselt | Martelarenlaan 42 | BE 3500 Hasselt



2024
2025

Faculteit Industriële Ingenieurswetenschappen

master in de industriële wetenschappen: energie

Masterthesis

Optimization of thin film chalcogenide solar cell baseline process

Nick Keppens

Scriptie ingediend tot het behalen van de graad van master in de industriële wetenschappen: energie

PROMOTOR :

Prof. dr. Bart VERMANG

PROMOTOR :

prof. dr. Guy BRAMMERTZ



KU LEUVEN

Preface

This master's thesis represents the culmination of my study at the joint program of Hasselt University and KU Leuven. The work presented here is about a topic that aligns with the growing global need for efficient and accessible renewable energy technologies. The urgency and importance of this global challenge are what initially drew my interest to the subject. Contributing to innovative and sustainable solutions with real-world impact is a goal that I consider both meaningful and professionally fulfilling.

It has been both a challenging and enriching journey, filled with learning experiences that have deepened my understanding of thin-film photovoltaics and experimental research.

My deepest gratitude goes out to my promoters, Prof. Dr. Guy Brammertz and Prof. Dr. Bart Vermang, for their important advice, encouragement and helpful criticism during the process of my research. This effort was strongly influenced by their expertise and support.

I am also thankful to all the colleagues at the lab for their assistance and for generously sharing their knowledge with me. My sincere appreciation goes out to my family and friends for their support and motivation throughout this academic journey.

This thesis would not have been possible without the collective influence of the people who have supported me along the way and I am deeply grateful for all the contributions that helped bring this work together.

Contents

| | |
|---|-----------|
| Preface | 1 |
| List of tables | 5 |
| List of figures | 7 |
| Glossary..... | 9 |
| Abstract | 11 |
| Abstract in Dutch | 13 |
| 1 Introduction | 15 |
| 1.1 Context | 15 |
| 1.2 Problem statement..... | 15 |
| 1.3 Objectives | 16 |
| 1.4 Materials and methods..... | 16 |
| 1.5 Preview | 17 |
| 2 Literature study | 19 |
| 2.1 Layer structure of CIGS cells | 19 |
| 2.1.1 The substrate | 19 |
| 2.1.2 The back contact..... | 20 |
| 2.1.3 The absorber layer | 20 |
| 2.1.4 The buffer layer | 20 |
| 2.1.5 The window layer | 20 |
| 2.2 Deposition methods for CIGS absorbers | 21 |
| 2.2.1 Vacuum-based methods | 21 |
| 2.2.2 Non-vacuum-based methods | 23 |
| 3 Experiment..... | 25 |
| 3.1 Full factorial design of experiments..... | 25 |
| 3.1.1 Fabrication of Absorber layer | 25 |
| 3.1.2 Characterization of absorber layer | 27 |
| 3.1.3 Characterization of solar cell | 30 |
| 3.1.4 Data analysis software | 32 |
| 3.1.5 Results and discussion | 33 |
| 3.2 Silver alloyed absorber layer | 40 |
| 3.2.1 Results and discussion | 41 |
| 3.3 Zinc oxysulfide buffer layer..... | 41 |
| 3.3.1 Results and discussion | 41 |
| 4 Conclusion..... | 43 |
| 4.1 Full factorial design | 43 |
| 4.2 Small-scale side experiments..... | 43 |

| | |
|-------------------------|-----------|
| References..... | 45 |
| Appendix A | 47 |
| Appendix B | 48 |
| Appendix C | 49 |

List of tables

| | |
|--|----|
| Table 1: FFD parameters | 27 |
| Table 2: Full experimental matrix | 33 |
| Table 3: Statistical significance of parameters FFD | 34 |
| Table 4: Settings for optimal efficiency | 34 |
| Table 5: Optimal settings for lifetime | 35 |
| Table 6: Optimal settings for peak wavelength | 36 |
| Table 7: New baseline configuration | 40 |
| Table 8: Predicted output variables based on the new baseline recipe | 40 |
| Table 9: Old baseline for selenization process..... | 40 |
| Table 10: Results samples alloyed with Ag | 41 |
| Table 11: Results samples with Zn(O,S) buffer layer | 42 |
| Table 12: Parameter settings of one-factor-at-a-time experiment for a Zn(O,S) buffer layer | 44 |

List of figures

| | |
|---|----|
| Figure 1: As-One furnace for the selenization step [4]..... | 16 |
| Figure 2: Measuring devices | 16 |
| Figure 3: Representation of the layer structure of CIGS solar cells [7, p.2] | 19 |
| Figure 4: Experimental setup for co-evaporation of CIGS solar cells [9, p.277] | 21 |
| Figure 5: Two-step process consisting of metal precursor sputtering followed by selenization [9, p.278] | 22 |
| Figure 6: Overview of solution-based deposition techniques used for ink deposition [15, p.3] ... | 23 |
| Figure 7: Metal layer stack after the sputtering step | 25 |
| Figure 8: Setup Annealsys As-One furnace | 26 |
| Figure 9: Baseline temperature-flow-time graphic [19, p.26] | 27 |
| Figure 10: Peak wavelength measurement (PV24-27-13a)..... | 28 |
| Figure 11: Lifetime measurement (PV24-27-13a)..... | 29 |
| Figure 12: SEM image at a magnification of 10 kx (PV24-27-13a)..... | 29 |
| Figure 13: Energy-dispersive X-ray spectroscopy measurement (PV-24-27-13a) | 30 |
| Figure 14: Dark curve I-V measurement (PV24-27-13a) | 31 |
| Figure 15: Illuminated curve I-V measurement (PV24-27-13a) | 32 |
| Figure 16: Actual by predicted plot for efficiency | 35 |
| Figure 17: Actual by predicted plot for lifetime | 36 |
| Figure 18: Actual by predicted plot for peak wavelength | 37 |
| Figure 19: Actual by predicted plot for Voc | 37 |
| Figure 20: Actual by predicted plot for Jsc | 38 |
| Figure 21: Actual by predicted plot for FF | 39 |

Glossary

| | |
|---|-------------------------------|
| Ag: Silver | 40-41,43 |
| c-Si: Crystalline silicon | 15 |
| CdS: Cadmium sulfide..... | 20,25,41,43 |
| CIGS: Copper indium gallium disulfide diselenide $\text{Cu}(\text{In,Ga})(\text{Se})_2$ | 15-17,19-24,29,40,43 |
| Cu: Copper | 15,20-22,24-25,30,39 |
| EU: European Union | 15 |
| FF: Fill factor | 19,25,30,38-41 |
| FFD: Full factorial design | 17,25,27,32-34,40-41 |
| Ga: Gallium..... | 15,20-22,24-25,28,30,39,41,43 |
| H_2S : Hydrogen sulfide | 22,26 |
| I-V: Current-voltage | 16,30-32 |
| In: Indium..... | 15,20-22,24-25,30,39 |
| IZO: Indium-doped Zinc Oxide | 20,25 |
| J_{sc} : Short-circuit current density | 25,30,38,40,41,43 |
| Mo: Molybdenum | 20,25 |
| Na: Sodium | 19,20 |
| N_2 : Nitrogen..... | 24,26 |
| PL: Photoluminescence spectroscopy | 16,27-28 |
| S: Sulphur | 30,39,41 |
| Se: Selenium..... | 15,20-26,30,39 |
| SEM: Scanning electron microscopy | 16,27,29-30 |
| SLG: Soda-lime glass..... | 19,25 |
| V_{oc} : Open-circuit voltage | 19-20,25,30,37-38,40-41 |
| $\text{Zn}(\text{O,S})$: Zinc oxysulfide | 20,41,43-44 |

Abstract

The drive towards climate neutrality in the EU by 2050 underscores the importance of advancing renewable energy technologies such as CIGS thin-film solar cells. This master's thesis focuses on improving the selenization step of the two-step process that is used to create the absorber layer of CIGS cells. The imo-imomec group's CIGS solar cells exhibit a relatively low efficiency of around 10 to 15%, compared to the best CIGS solar cell which achieves 23.6%. There is therefore a need to further enhance the efficiency with more process optimizations.

Building upon previous work that established the current baseline recipe, four key process parameters were identified as significantly influencing the overall performance of CIGS solar cells. To investigate the combined effects of these variables and to identify their optimal settings, a full factorial design of experiments approach was employed for the crystallization process of the CIGS absorber.

The selenization step was carried out using an Annealsys AS-One furnace. For the characterization of the CIGS solar cells, PL-, SEM-, and I-V measurements were employed. The measurement results were analyzed using JMP 6 statistical software. Based on the FFD, a mathematical model was developed to quantify the effects and interactions of the process parameters on device performance.

The statistical analysis revealed that only three of the four parameters had a significant influence, while interactions between the parameters were found to be statistically insignificant. For the output parameters, the influence was limited to the peak wavelength and J_{sc} . However, the overall solar cell efficiency remains insufficient. The findings suggest that further optimization should target the metal sputtering step preceding the selenization process.

Abstract in Dutch

Het streven naar klimaatneutraliteit in de EU tegen 2050 benadrukt het belang van geavanceerde technologieën voor hernieuwbare energie, zoals CIGS dunne-film zonnecellen. Deze masterproef focust op het verbeteren van de selenisatie stap van het twee-staps proces dat gebruik wordt om de absorbeerlaag van CIGS cellen te maken. De CIGS zonnecellen van de imo-imomec groep vertonen een relatief lage efficiëntie van ongeveer 10%, in vergelijking met de beste CIGS zonnecel die 23,6% haalt. Daarom is het nodig om de efficiëntie verder te verbeteren met meer procesoptimalisaties.

Voortbouwend op eerder werk dat het huidige basisrecept vaststelde, werden vier belangrijke procesparameters geïdentificeerd die de algemene prestaties van CIGS zonnecellen significant beïnvloeden. Om de gecombineerde effecten van deze variabelen te onderzoeken en hun optimale instellingen te identificeren, werd een full factorial design of experiments toegepast op het kristallisatieproces van de CIGS absorber.

De selenisatie stap werd uitgevoerd met behulp van een Annealsys As-One oven. Voor de karakterisering van de CIGS zonnecellen werden PL-, SEM-, en I-V metingen uitgevoerd. De meetresultaten werden geanalyseerd met JMP 6 statistische software. Op basis van de FFD werd een wiskundig model ontwikkeld om de effecten en interacties van de procesparameters op de prestaties van het apparaat te kwantificeren.

Uit de statistische analyse bleek dat slecht drie van de vier parameters een significante invloed hadden, terwijl de interacties tussen de parameters statistisch niet significant bleken te zijn. Voor de outputparameters was de invloed beperkt tot de piekgolflengte en J_{sc} . De totale efficiëntie van de zonnecellen blijft echter onvoldoende. De bevindingen suggereren dat verdere optimalisatie zich zou moeten richten op de metaalsputterstap, voorafgaand aan het selenisatieproces.

1 Introduction

1.1 Context

The transition to renewable energy is an essential part of Europe's climate goals, with the European Union (EU) aiming for climate neutrality by 2050. Solar energy and other renewable energy sources are essential to this transformation. By aiming for 42.5% of the overall energy mix to be produced from renewables by 2030, the EU has increased its target for renewable energy. [1]

To achieve this objective, thin-film solar cells, specifically Copper Indium Gallium Diselenide Cu(In,Ga)(Se)_2 (CIGS) cells play a major role. Although the lower cost of Crystalline Silicon (c-Si) technology, CIGS still offers some benefits. Because CIGS solar cells are more sensitive to light, they have lower power losses. This results in CIGS modules producing more power than c-Si modules at low irradiance. Furthermore, c-Si technology is mostly utilized for rooftop applications and solar parks, while CIGS technology has a wider range of uses like flexible photovoltaic modules, building-integrated photovoltaics, and solar shingles. [2]

At the Energyville campus in Genk, the imo-imomec research group of imec and Hasselt university is conducting research on optimizing these CIGS-based solar cells. The goal of this master's thesis is to improve the selenization step of the two-step process that is used to fabricate the absorber layer. This two-step process involves first depositing a metallic precursor stack containing Copper Gallium CuGa and Indium In followed by annealing this metal stack in an atmosphere of Selenium (Se), which is also called the selenization process. Through this process, the metal stack is transformed into the CIGS absorber layer, which is crucial to the solar cell's functionality.

1.2 Problem statement

At the start of the thesis, CIGS solar cells produced from the imo-imomec research group had an average energy conversion efficiency of 10%. In comparison, the world's most efficient CIGS cell has an efficiency of 23.6% [3]. This highlights that significant optimizations are needed to approach the performance of this champion cell. In the process of improving the cells, additional problems will be faced. One common issue is non-uniformity in the film, where variations in thickness or composition can lead to inconsistent efficiency across the cell. Another problem is that cracks can appear in the absorber layer.

1.3 Objectives

The primary goal of this master's thesis is to raise the average power conversion efficiency of the imomomec group's CIGS solar cells to a target of at least 15%. In addition to reaching this efficiency level, it is essential to ensure that the developed baseline process is stable and free from mechanical defects, thereby guaranteeing the reproducibility and reliability of the solar cells.

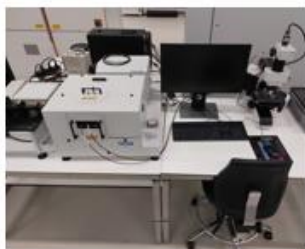
To achieve this goal, the thesis will focus on investigating the influence of key process parameters during the selenization of the absorber layer. The parameters of interest include the ramping speed, anneal temperature, total anneal time, and post-anneal time. By analyzing the impact of these parameters on the solar cell characteristics, the aim is to identify an optimal combination that leads to improved efficiency.

1.4 Materials and methods

First, a literature review is necessary to gain a deep understanding of the manufacturing methods of CIGS solar cells. Additionally, it is crucial to understand how different modifications in the process affect the formation and properties of the absorber layer. This is complemented by training on the selenization process used for creating of the absorber layer (see Figure 1), as well as training on key characterization techniques for determining material quality and the electrical properties, such as Photoluminescence Spectroscopy (PL), Scanning Electron Microscopy (SEM) and Current-Voltage (I-V) measurements (see Figure 2). These characterization methods are further explained in Chapter 3 under Characterization of absorber layer and Characterization of solar cell.



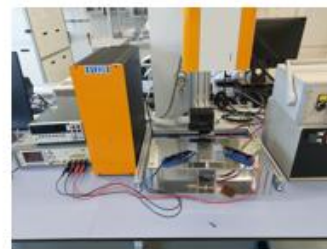
Figure 1: As-One furnace for the selenization step [4]



a) PL



b) SEM [5]



c) I-V setup

Figure 2: Measuring devices

After this training, initial experiments are performed to gain experience in the fabrication of the absorber layer. The CIGS solar cells are fabricated using various optimization approaches, where the energy conversion efficiency is measured by current-voltage measurements.

After the initial phase, a Full Factorial Design (FFD) with four parameters is established. A FFD is a specific type of design of experiments in which all possible combinations of factor levels are tested. It is a systematic approach that examines the individual effects and interactions of input variables on output responses. [6]

The solar cells are characterized using the previously mentioned techniques. The measurement data are analyzed using JMP 6 statistical software. The software provides a mathematical model that quantifies the individual effects and interactions of the selected process parameters related to the solar cell's performance.

1.5 Preview

A literature study of the layer structure of CIGS solar cells and the various deposition methods utilized to create the absorber layer is provided in the next chapter. The following chapter outlines the experimental setup and describes the results. Finally, the results are analyzed and interpreted to determine how the process parameters affect the solar cell's performance.

2 Literature study

2.1 Layer structure of CIGS cells

Figure 3 illustrates the standard structure of a CIGS solar cell. The structure consists of five different layers arranged sequentially from bottom to top. These layers are in order: the substrate, the back contact, the absorber layer, the buffer layer and the window layer [7].

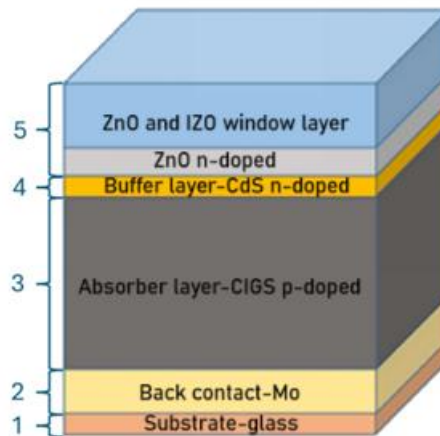


Figure 3: Representation of the layer structure of CIGS solar cells [7, p.2]

2.1.1 The substrate

The entire stack of CIGS solar cells is mechanically supported by the substrate. The most commonly used substrate is Soda-Lime Glass (SLG) due to its thermal stability, chemical compatibility, and ability to provide the absorber layer with Sodium (Na) during the co-evaporation or selenization processes. It has been proven that adding Na at a concentration of 0.1 at% (atomic percent) significantly enhances the CIGS solar cell's performance [8]. This improvement is primarily observed in the Open-Circuit Voltage (V_{OC}) and Fill Factor (FF), leading to an overall increase in solar cell efficiency. The role of Na is mainly responsible for this increase in efficiency, because Na reduces defects at the junction between the buffer and absorber layer. Moreover, SLG meets most of the necessary criteria, including strong adhesion, lightweight properties and compatibility with temperatures above 500°C , which are essential for achieving the high process temperatures required for crystallizing the CIGS absorber layer [8]. Alternative substrates include flexible polymers, steel, and ceramics, each with specific advantages and trade-offs. The choice of substrate directly affects the processing conditions, especially the selenization step, and is important for the overall efficiency and mechanical properties of the solar cells. [7], [8]

2.1.2 The back contact

The back contact consisting of a Molybdenum (Mo) layer, typically around 500 nm thick, is deposited onto the substrate [7]. It serves as an optical reflector in CIGS solar cells, that reflects unabsorbed photons back into the absorber layer, which improves the solar cell's efficiency [8]. Although alternative materials, such as tungsten (W), tantalum (Ta), niobium (Nb), chromium (Cr), vanadium (V), titanium (Ti) and manganese (Mn), can also be employed for the back contact, Mo is the preferred material due to its chemical stability, high conductivity, and the formation of a Molybdenum diselenide (MoSe_2) interfacial layer, which ensures an excellent ohmic contact with the absorber layer [8]. Also, the structure of the Mo layer facilitates Na to diffuse into the absorber from the glass, which is crucial for enhancing solar cell efficiency. [7], [8], [9]

2.1.3 The absorber layer

Sunlight is absorbed by the absorber layer, which generates electron-hole pairs. CIGS solar cells are named after the elements in the absorber layer, namely Cu, In, Ga and Se. The CIGS absorber is a p-type semiconductor typically 1.5–2.5 μm thick [9]. The bandgap is tunable from 1.014 eV for CuInSe_2 to 1.697 eV for CuGaSe_2 by adjusting the Ga/(Ga+In) ratio [7]. At a composition ratio of 0.3, the semiconductor has a bandgap of 1.1-1.2 eV, which is optimal for efficient solar energy conversion [7]. Because of its high absorption coefficient in the absorber, it can be used in thin-film layers. [7], [9]

2.1.4 The buffer layer

The Cadmium Sulfide (CdS) buffer layer is a thin n-type semiconductor of 50-80 nm [9]. It forms a p-n junction with the underlying p-type absorber layer, enabling the separation of charge carriers. With a slightly wider bandgap than the absorber, the buffer layer allows incoming photons to pass through and reach the absorber layer. Additionally, the buffer layer is necessary for improving the V_{OC} , band structure and reducing tunneling effects. Furthermore, it protects the absorber layer from mechanical damage that could happen during the deposition of the top contact window layers. Usually, the buffer layer is composed out of CdS , but because cadmium is toxic, other materials such as Zinc Oxysulfide (Zn(O,S)) are being explored. [7], [9]

2.1.5 The window layer

The window layer enables light transmission to the absorber, while collecting electrons. It typically consists of a thin Zinc Oxide layer of around 50 nm to reduce electronic losses [7]. On top of this thin layer, comes a thicker aluminum-doped zinc oxide layer of 200-400 nm for efficient charge collection [7]. This aluminum-doped layer can also be replaced with other materials like indium-doped tin oxide (ITO) and Indium-doped Zinc Oxide (IZO). [7], [10]

2.2 Deposition methods for CIGS absorbers

Different thin-film deposition techniques can be used for the growth of CIGS absorbers, which are divided into two main groups: vacuum-based and non-vacuum-based techniques. Despite producing excellent absorber layers, vacuum-based methods require a significant initial investment in equipment for manufacturing. Conversely, non-vacuum methods are cost-effective and relatively straightforward. However, the resulting absorber layers generally exhibit lower quality and performance compared to those produced by vacuum-based techniques, the criteria for selecting an appropriate deposition method vary between laboratory-scale and commercial-scale applications. Laboratory-scale processes prioritize precise control over the composition and properties of CIGS films to maximize cell efficiency. In commercial manufacturing, the focus is on process tolerance, high throughput, reproducibility and cost efficiency. [9]

2.2.1 Vacuum-based methods

The two most popular vacuum-based methods for fabricating CIGS solar cells are the ones that have shown great efficiency of the devices efficiencies and are utilized in commercial manufacturing. These two approaches are the co-evaporation method and the two-step process. [9]

2.2.1.1 Co-evaporation processes

One commonly used approach for the deposition of CIGS absorber layers is co-evaporation. This approach includes the thermal evaporation of the elements Cu, In, Ga and Se from individual sources onto the substrate. The source temperature of the elements varies on the melting temperature of the elements, with Cu typically evaporates at 1300-1400 °C, In at 1000-1100 °C, Ga at 1150-1250 °C and Se at 300-350 °C [9]. Figure 4 shows the typical laboratory setup used for co-evaporation, in which the evaporated elements are heated so that they grow on the substrate. Due to the high adhesion coefficients of Cu, In and Ga, the growth rate of the absorber layer is mainly determined by the outflow of these metals. Because Se has a higher vapor pressure and a lower sticking coefficient, it typically evaporates more than is needed. [9]

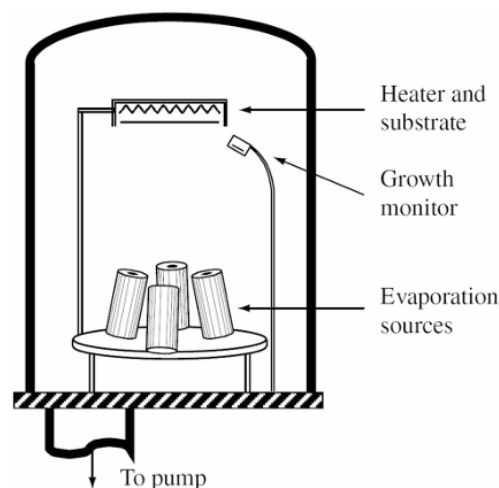


Figure 4: Experimental setup for co-evaporation of CIGS solar cells [9, p.277]

In order to control the Cu profile during film growth, three main types of the co-evaporation process are developed [11]. In all co-evaporation processes, the Se flux is maintained constant [9]. These three types are the following:

1. Single-stage process: this method maintains constant fluxes of all elements throughout the process, ensuring a Cu-poor environment. It offers simplicity and good control over composition, although it usually results in smaller grain sizes. [9]
2. Two-stage process (Boeing process): in the first stage a Cu-rich composition is used to grow the film, which develops big grains. Then, Cu flux is decreased and In and Ga fluxes are increased to achieve a slightly Cu-poor film, which results in grain growth promotion. [9]
3. Three-stage process: this process begins with the deposition of In and Ga, followed by a Cu flux to achieve a Cu-rich composition. The final stage deposits In and Ga to return the composition back to a slightly Cu-poor state. This approach enables precise control over composition and facilitates the formation of graded bandgap structures. Using the three-stage process, the highest efficiencies were obtained. [9], [11]

The ability to modify the absorber's composition and bandgap across thickness is a key benefit of the co-evaporation process. The main disadvantage of this process is the challenge of managing the evaporation sources, which requires advanced control and diagnostics. [9]

2.2.1.2 Two-step process

The two-step process shown in Figure 5 is another popular technique for forming the absorber layer of CIGS solar cells. This process consists of two primary steps:

1. Precursor deposition: the metals Cu, In and Ga are first deposited on a substrate, usually done by sputtering. Cu, In and Ga metal precursors are often deposited via sputtering, either from a compound Cu(InGa)Se_2 target, from an alloy CuInGa target or from distinct CuGa and In targets [9]. Both sequential and co-sputtering are methods for sputtering from separate CuGa and In targets. Of these methods, co-sputtering achieves the best results. [9]
2. Selenization: the metal stack is then heated in a Se containing atmosphere of 400-600 °C [9], [11]. Se is introduced either as elemental Se vapor or highly reactive and toxic hydrogen selenide (H_2Se) gas. During this step the metal stack reacts with the Se and forms a crystalline CIGS absorber. [9], [12]

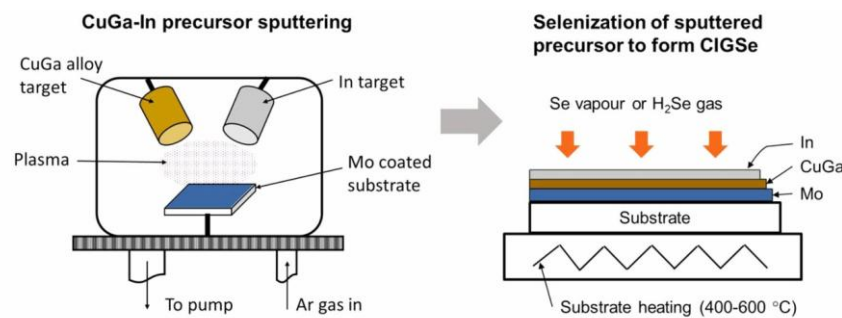


Figure 5: Two-step process consisting of metal precursor sputtering followed by selenization [9, p.278]

2.2.2 Non-vacuum-based methods

The non-vacuum methods, including solution-processing, electrodeposition and spray coating, present a cost-effective and scalable alternative to traditional vacuum-based techniques for producing CIGS absorber layers [13]. These methods simplify and lower the cost of processing large devices by lowering capital investment and equipment complexity. [9]

2.2.2.1 Solution-processing

Solution-processing is a promising low cost and viable for commercial scale method for fabricating CIGS absorbers [9], [14]. The first step of the process is the preparation of the ink. “Particulate ink can be prepared in many ways like dissolving nanoparticles of metals or metal oxides or selenides, etc. which are then printed onto a suitable substrate, chemical synthesis of nanoparticles of desirable materials, thereby dispersing them in apposite solvent to form ink.” [9, p.281]. A range of methods used for applying precursor inks are presented in Figure 6.

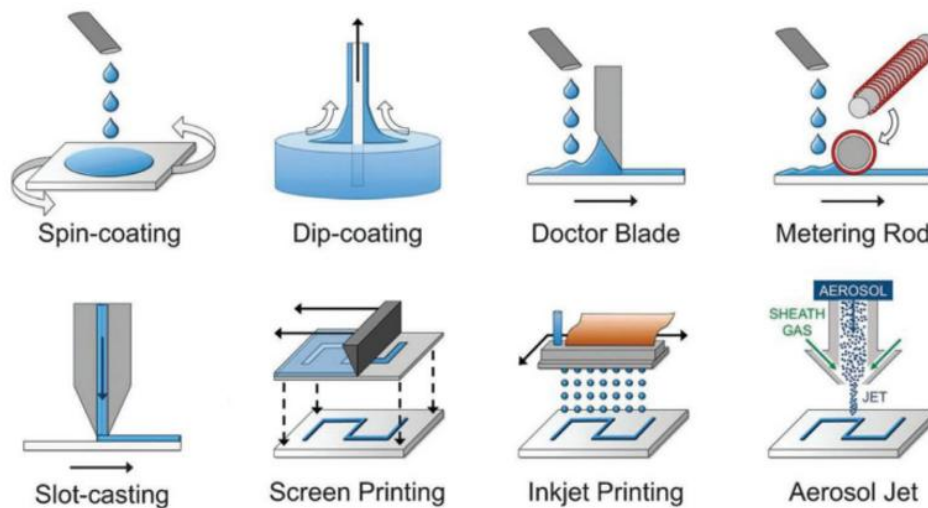


Figure 6: Overview of solution-based deposition techniques used for ink deposition [15, p.3]

After the ink is deposited on the substrate, the samples must be annealed in a Se atmosphere. This procedure can be compared to the selenization step of the previously mentioned two-step process. [9], [14], [15]

2.2.2.2 Electrodeposition

Another non-vacuum method for creating CIGS absorbers is electrodeposition. This is an ideal alternative for vacuum methods, because of its low cost, scalability and suitability for roll-to-roll production on large substrates of every shape. This method involves reducing metal ions onto a substrate by applying a constant or pulsed voltage or current in a solution with the desired precursor ions. [9], [16]

However, because the reduction potentials of the different elements vary significantly, electrodeposition is challenging for compounds such as CIGS. As a result, element deposition is often carried out with the deposition potentials selected for each element separately according to their reduction potentials. To obtain high-quality films and minimize the numbers of processing steps, it is preferable to co-deposit all components simultaneously. After the deposition, the sample is annealed in a Se atmosphere to convert it into a CIGS absorber suitable for photovoltaic applications. [9], [16]

2.2.2.3 Spray coating

The last technique discussed is spray coating. Like the other non-vacuum methods also divided in two steps. First a precursor solution containing Cu, In and Ga metal salts is dissolved in a solvent mixture of ethanol and deionized water. During deposition, the precursor solution atomized using an ultrasonic generator to create a fine mist. This mist is carried out by Nitrogen (N_2) gas onto the heated substrate of around 400 °C, for better deposition [17]. Following deposition, the deposited substrate undergoes a selenization step to form the absorber. Despite its simplicity, versatility and low cost, this method struggles to ensure uniform film thickness on the substrate [18]. [17]

3 Experiment

3.1 Full factorial design of experiments

This master's thesis used a FFD in which four parameters of the selenization process were systematically varied. This design allowed the creation of a mathematical model that described the effects and interactions of these parameters on the cell performance.

The process parameters that were varied include the ramping speed, anneal temperature, total anneal time and post-anneal time. To evaluate the performance of the solar cells, several characteristics were measured: composition of elements, the peak position, the lifetime, as well as the electrical parameters J_{sc} , V_{oc} , FF and efficiency.

For this experiment, a SLG substrate with a thickness of 3 mm was used. A Mo back contact layer with a thickness of 500 nm was deposited on top of it. The absorber layer was then applied, as described in (3.1.1). On top of the absorber layer, a 50 nm thick CdS buffer layer was deposited. Finally, the stack was completed with the window layer, which consisted out of a 30 nm thick ZnO layer and a 150 nm thick IZO layer.

3.1.1 Fabrication of Absorber layer

The absorber layer was fabricated using a two-step process. This first step was carried out at HTC Eindhoven, where the metal deposition took place. Initially, Cu and Ga were sputtered together on the substrate at 30 °C, followed by In sputtering at 150 °C. This sequence was repeated ten times, to create a CuGa/In layer of 800 nm. Following that, a Se layer with a thickness of 2-3 μm was deposited on top of the stacked CuGa/In layer. Figure 7 illustrates the layer stack after the metal sputtering step. [19]



Figure 7: Metal layer stack after the sputtering step

After the sputtering step, the total sheet was 30 cm by 30 cm. This sheet was then cut into individual samples of 2.5 cm by 5 cm. At this point, these samples were ready for the selenization step. Each sample was placed inside a graphite box as illustrated in Figure 8, which was then loaded into the Annealsys As-One furnace. A graphite box was used to contain the Se vapor and control its distribution [20]. A thermocouple was then attached to the graphite box to measure the sample temperature, which was crucial for accurate process control.

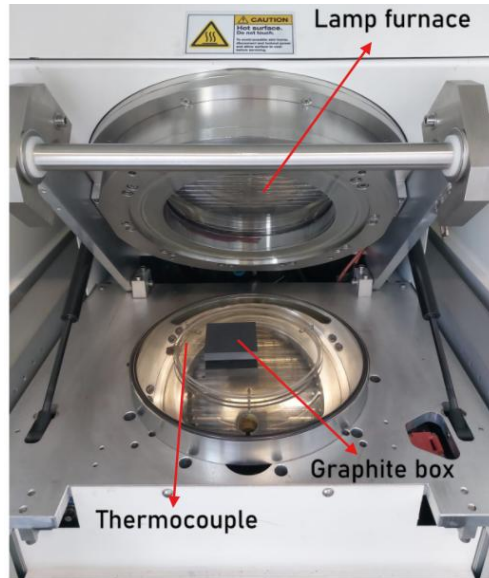


Figure 8: Setup Annealsys As-One furnace

A graph of the selenization process is shown in Figure 9 and consists of the following steps:

- Venting and pumping (1): The selenization process begins with a chamber cleaning sequence consisting of a N_2 purge at 800 mbar, followed by a H_2S purge at 30 mbar and finished with a second N_2 purge at 650 mbar. This procedure is implemented to prevent contaminations during the process. In order to prepare for the ramping stage, the chamber is kept at room temperature during this phase and is exposed to vacuum conditions. [19], [21]
- Ramping (2): The specified ramping speed determines how fast the chamber's temperature rises to the predefined annealing temperature during the ramping phase. This ramping speed is controlled by adjusting the lamp power. Throughout the entire ramping phase, a constant flow of 20 sccm H_2S is introduced into the chamber. This controlled gas flow helps stabilize the internal pressure and prevents overpressure during the heating process. [19], [21]
- Annealing (3): When the desired anneal temperature is reached, the annealing process starts. This step consists of two parts. First, the sample is annealed under a continuous H_2S flow of 20 sccm for a duration determined by the specified anneal time. Following this, the sample undergoes a second annealing phase of equal duration, but without the H_2S flow. [19], [21]
- Post-annealing (4): The temperature is maintained the same as in the previous step. At the beginning of this phase, a short H_2S purge is performed at 20 mbar. Following the purge, the sample is annealed for a predetermined duration without any H_2S flow. [19], [21]

- Cooling (5): In the final step, the lamp power is switched off, allowing the sample to cool down to 100 °C. Once this temperature is reached, the chamber undergoes a venting and pumping cycle to remove any residual gases. After this step, the sample can be safely removed from the furnace. [19], [21]

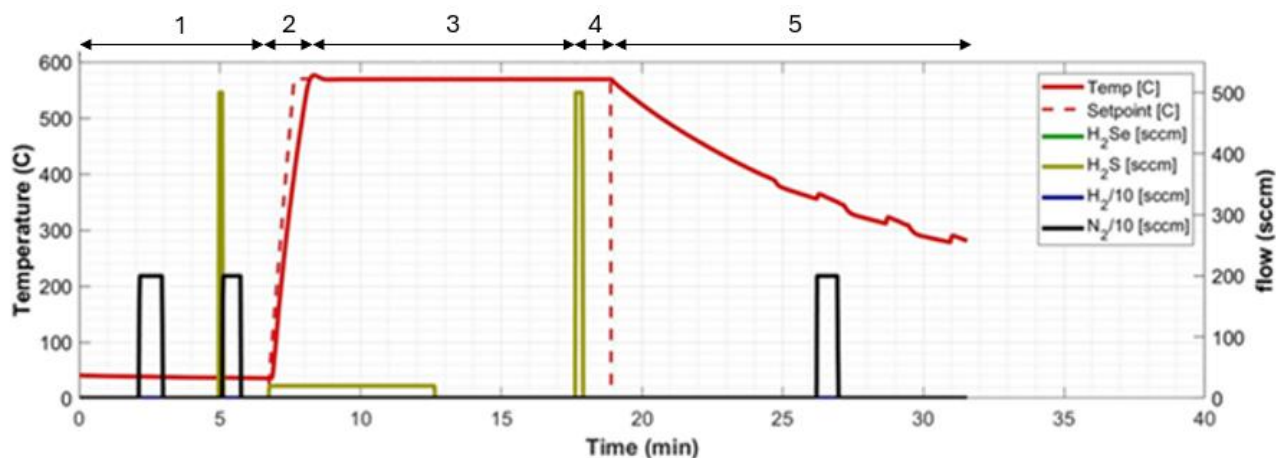


Figure 9: Baseline temperature-flow-time graphic [19, p.26]

All samples underwent the same steps of the selenization process, with the exception of four varied parameters: ramping speed, anneal temperature, total anneal time and post-anneal time. The specific values used for these parameters are shown in Table 1.

Table 1: FFD parameters

| Parameters | Unit | - | Baseline | + |
|--------------------|------|-----|----------|-----|
| Ramping speed | °C/s | 0.3 | 2 | 4 |
| Anneal temperature | °C | 530 | 545 | 560 |
| Total anneal time | min | 3+3 | 5+5 | 7+7 |
| Post-anneal time | min | 1 | 3 | 5 |

3.1.2 Characterization of absorber layer

After the absorber layer had been fabricated, the first characterization techniques were performed on the samples. At that stage, PL and SEM were the two techniques that could already be applied.

3.1.2.1 Photoluminescence spectroscopy

The PL setup is illustrated in Figure 2. For this experiment, the FluoTime 300 spectrometer was used in combination with the FluoMic microscope, both manufactured by PicoQuant. When a high-power He-Ne laser was directed onto the sample, the bandgap of the absorber layer could be determined [21]. Insight into the Ga integration in the absorber is provided with the bandgap. Additionally, lifetime measurements were carried out using the same setup to assess the quality of the absorber layer. To evaluate the uniformity of the sample, measurements were taken from multiple regions across each sample. [19], [21]

In Figure 10 a measurement of the wavelength is presented. The intensity was measured in steps of 5 nm throughout a spectral range of 800 nm to 1370 nm. From this measurement, the peak wavelength could be identified directly from the graph.

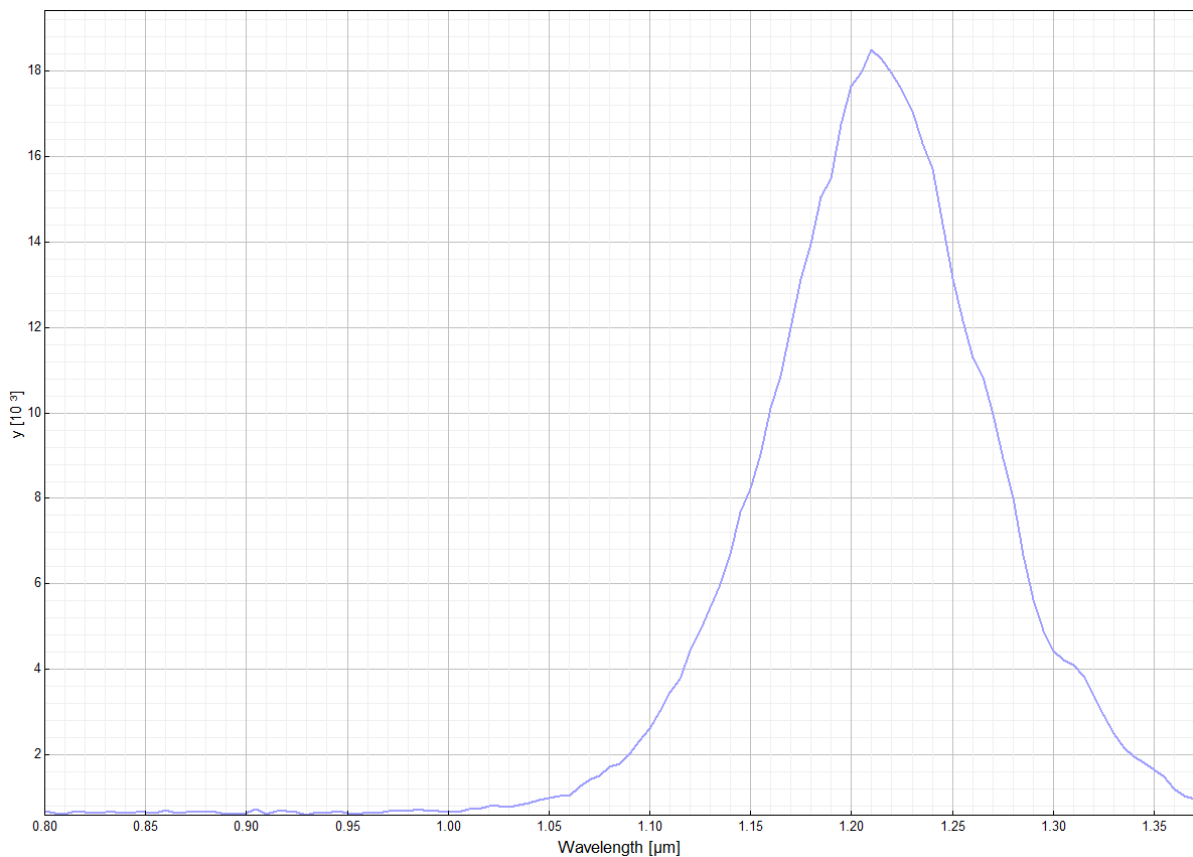


Figure 10: Peak wavelength measurement (PV24-27-13a)

The lifetime was determined by recording the time-resolved emission of photons, with the time axis divided into 1024 channels. The measurement continued until one of the channels accumulated 10 000 emitted photon counts. The recorded intensity decrease was analyzed using FluoFit software, which extracted the lifetime from the curve. Figure 11 shows a graph for the lifetime measurement.

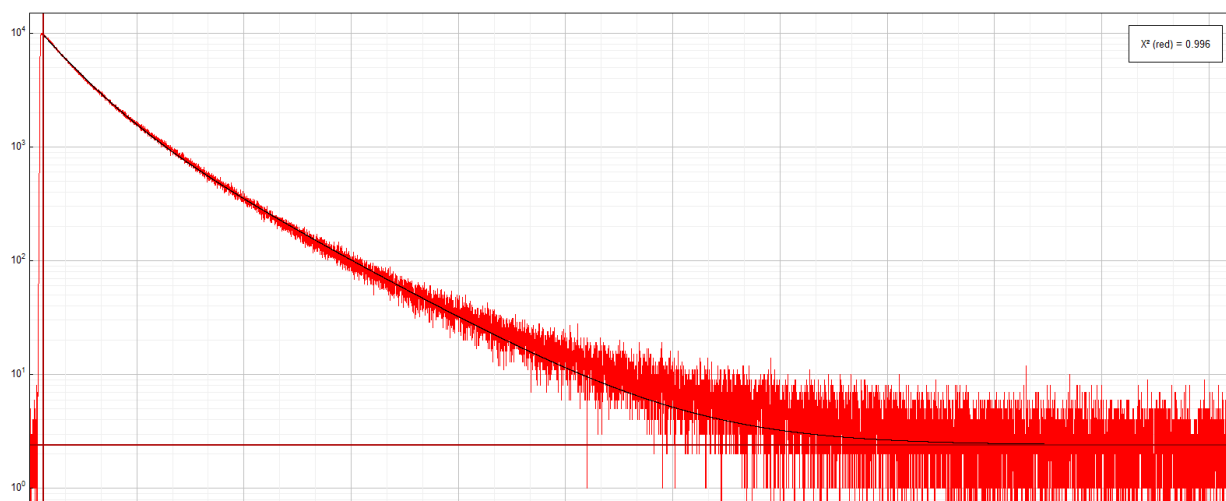


Figure 11: Lifetime measurement (PV24-27-13a)

3.1.2.2 Scanning electron microscopy

The SEM used in this study was the Vega3 SEM from Tescan, illustrated in Figure 2. SEM imaging allowed visualization of the microstructure of the CIGS absorber layer, enabling the identification of the grain size and structural defects such as cracks. The SEM images were captured at magnifications from 1 kx to 20 kx, using a beam intensity of 4 and an acceleration voltage of 15 kV. Figure 12 shows a SEM image taken at a magnification of 10 kx. [19], [21]

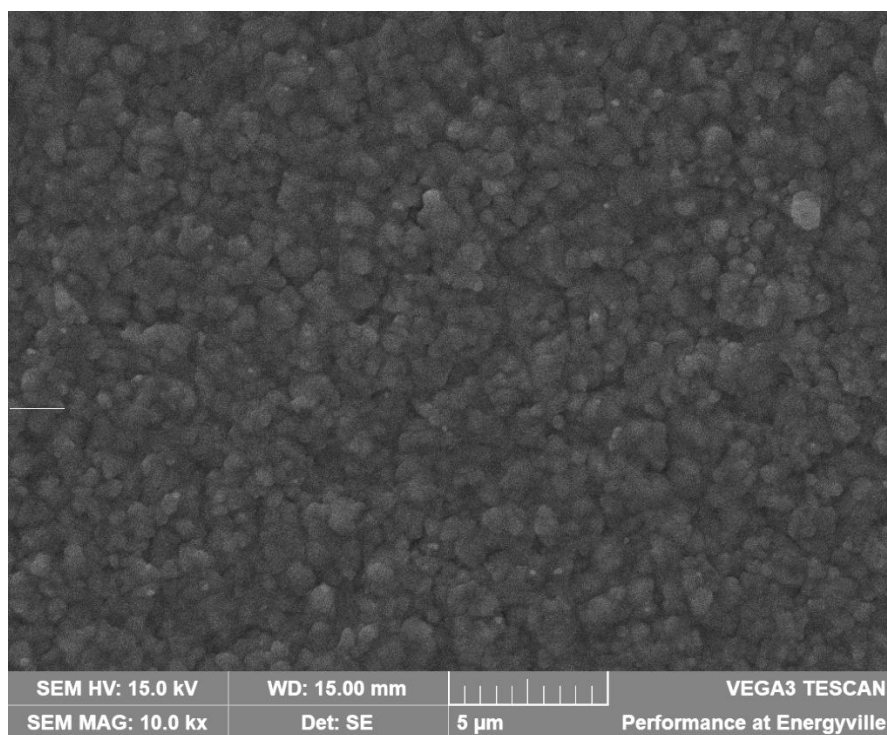


Figure 12: SEM image at a magnification of 10 kx (PV24-27-13a)

After capturing the SEM images, energy-dispersive X-ray spectroscopy measurements were performed to quantify the composition of the CIGS absorber. The ratios of the elements Cu, Ga, In, Se and Sulphur (S) were determined for the top layer of the absorber. These measurements were conducted using a beam intensity of 12 and an acceleration voltage of 15 kV. Figure 13 shows the result of an energy-dispersive X-ray spectroscopy measurement. [19], [21]

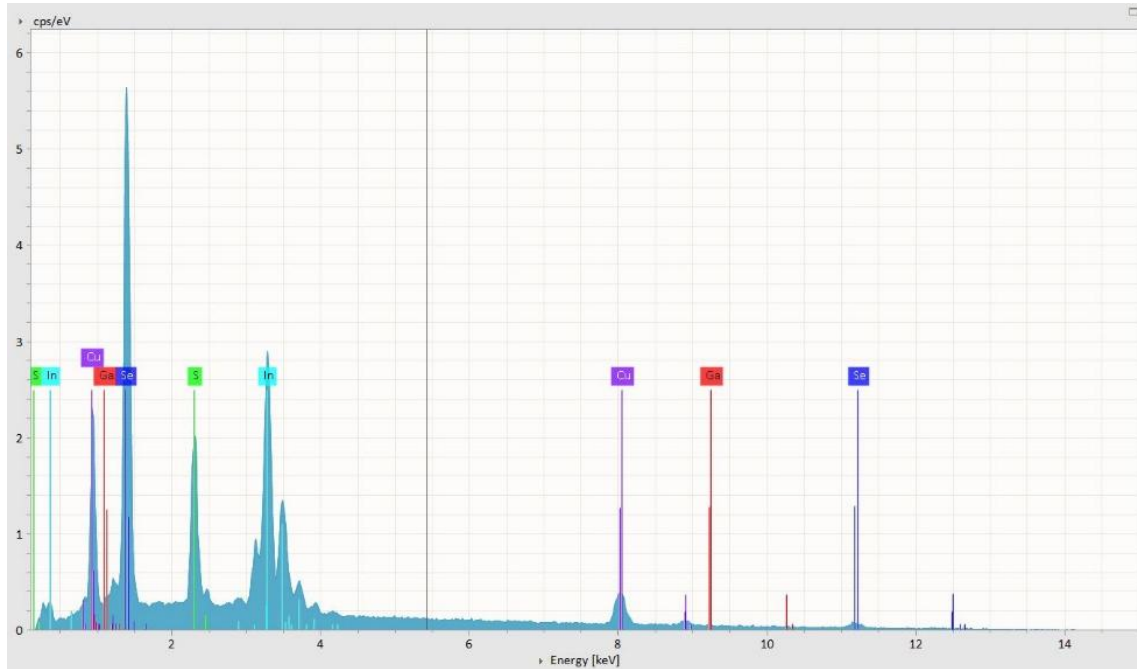


Figure 13: Energy-dispersive X-ray spectroscopy measurement (PV-24-27-13a)

3.1.3 Characterization of solar cell

Following the initial characterizations, the samples were further processed into full-fledged solar cells. Then, I-V measurements were performed on the fully developed solar cells.

3.1.3.1 Current-Voltage measurements

The final characterization technique used in this experiment was the I-V measurement, of which the setup shown in Figure 2. Before the measurement, the samples were annealed on a hot plate at 170 °C for 15 minutes. After annealing, the samples were placed under the SINUS-70 solar simulator from Wavelabs, which can produce the AM1.5 Global solar spectrum. This spectrum is similar to the sunlight at the earth's surface [22]. Two probes were placed on each sample, one to the solar cell's grid and the other to the back contact. Each cell was first measured twice under dark conditions (Figure 14), followed by seven measurements under illumination (Figure 15). During testing, the cell temperature was maintained at 25 °C. The resulting data was analyzed using Tracer software, providing electrical parameters such as J_{sc} , V_{oc} , FF and the efficiency. [19], [21]

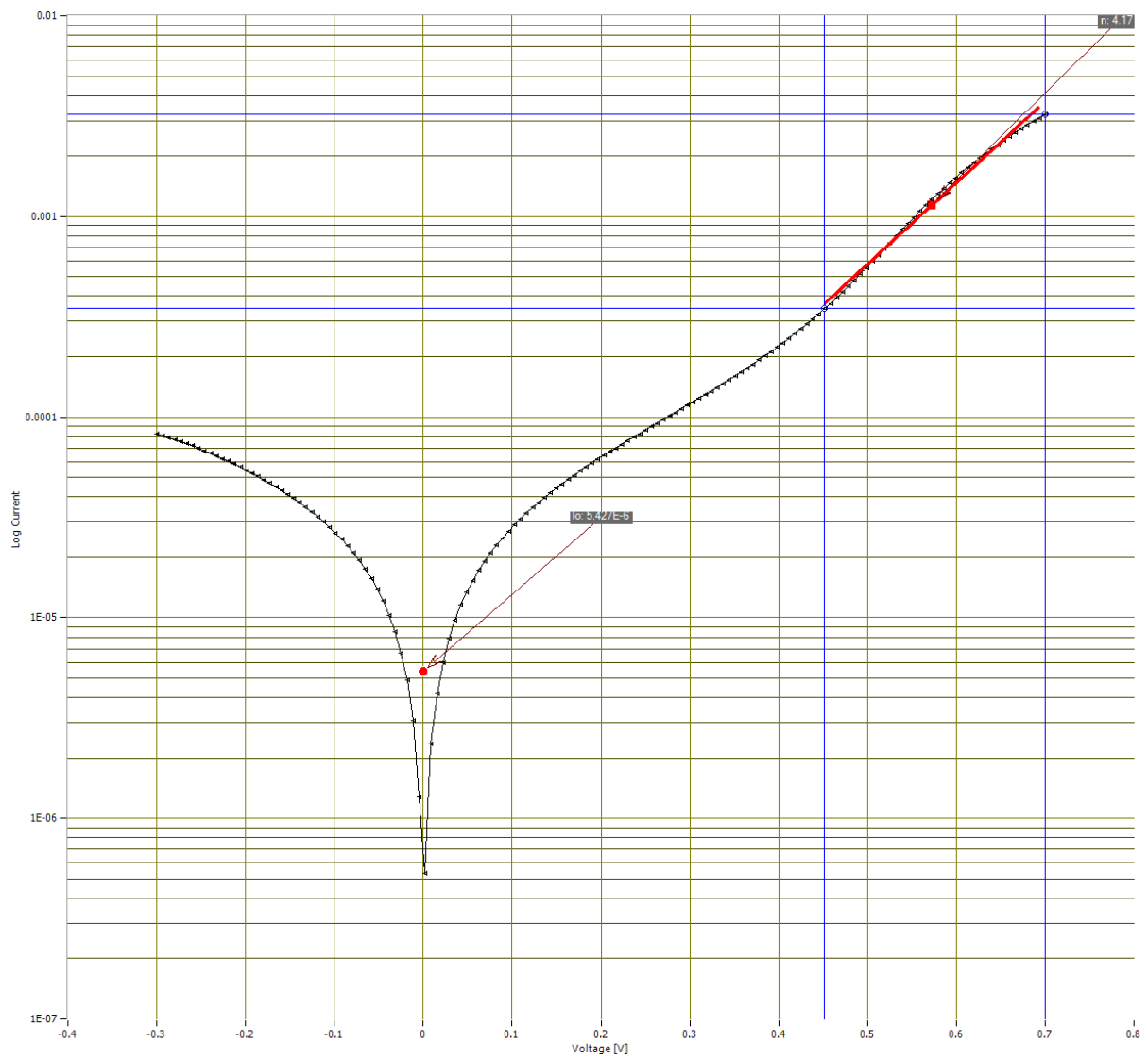


Figure 14: Dark curve I-V measurement (PV24-27-13a)

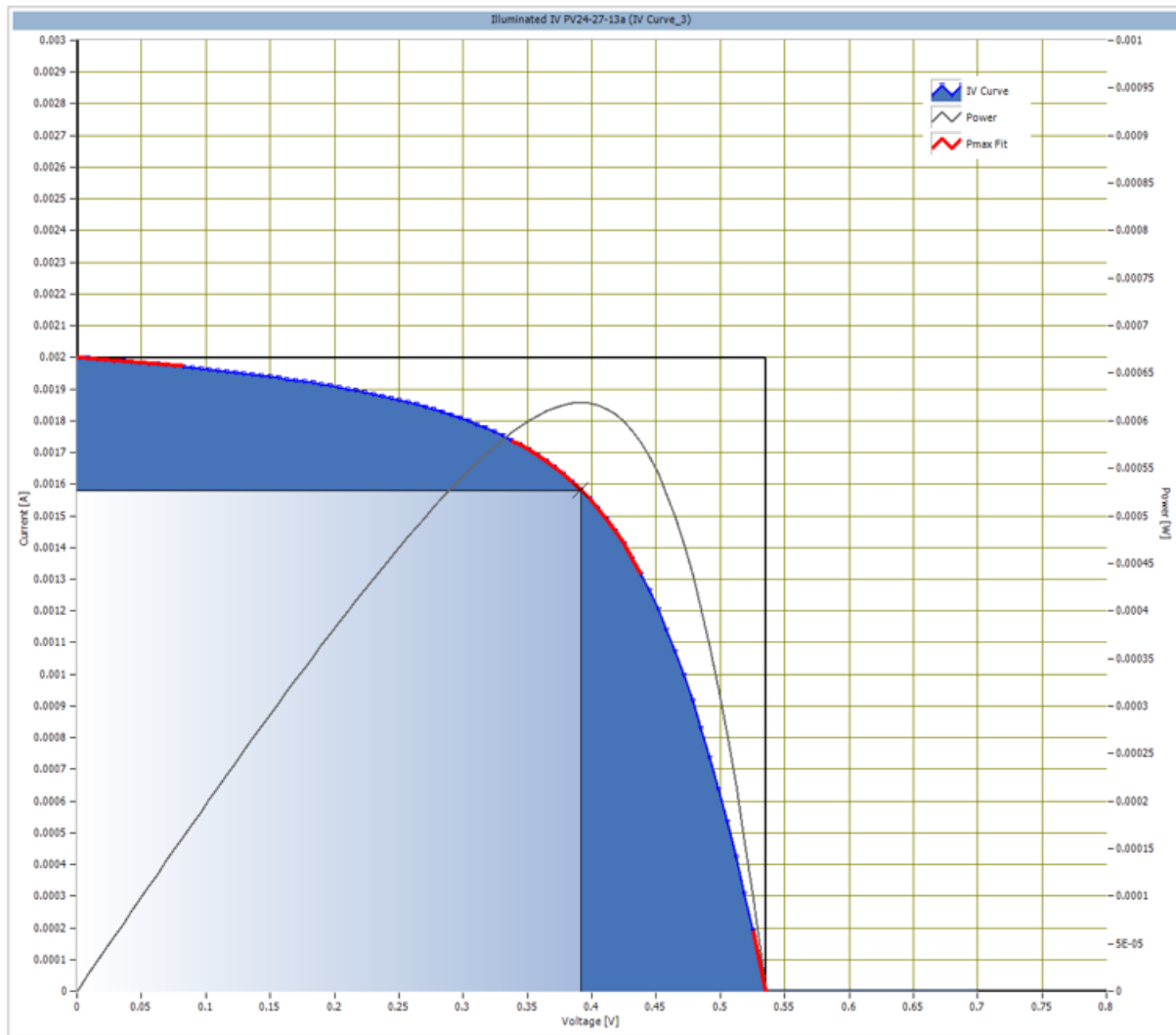


Figure 15: Illuminated curve I-V measurement (PV24-27-13a)

3.1.4 Data analysis software

All data obtained from the FFD experiment were analyzed using JMP 6 statistical software. This software generated a mathematical model that quantified the individual effects and interactions between the four varied process parameters. The output parameters were optimized within the software by applying a desirability function, which aimed to identify the optimal process parameters. In the software, all output parameters were set to equally important. The used data results are shown in Appendix A.

In Table 2, an overview of all experiments conducted in the FFD is presented, including repeated baselines (0) to assess reproducibility and estimate experimental error. In the description, a “+” indicates the highest value of a process parameter, while a “-” indicates the lowest. The sequence of symbols represents the following parameters in order: ramping speed, anneal temperature, total anneal time and post-anneal time.





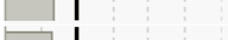
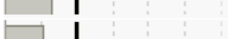
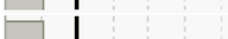
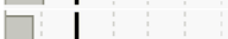

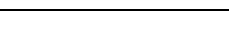
Table 2: Full experimental matrix

| Run | Description | Ramping speed | Anneal temperature | Total anneal time | Post-anneal time |
|-----|-------------|---------------|--------------------|-------------------|------------------|
| 1 | 0 | 2 °C/s | 545 °C | 5 +5 min | 3 min |
| 2 | ++-- | 4 °C/s | 560 °C | 3+3 min | 1 min |
| 3 | +--- | 4 °C/s | 530 °C | 3+3 min | 1 min |
| 4 | 0 | 2 °C/s | 545 °C | 5+5 min | 3 min |
| 5 | ---+ | 0.3 °C/s | 530 °C | 3+3 min | 5 min |
| 6 | ---- | 0.3 °C/s | 530 °C | 3+3 min | 1 min |
| 7 | 0 | 2 °C/s | 545 °C | 5+5 min | 3 min |
| 8 | ++-+ | 4 °C/s | 560 °C | 3+3 min | 5min |
| 9 | -+++ | 0.3 °C/s | 560 °C | 7+7 min | 5 min |
| 10 | --+- | 0.3 °C/s | 530 °C | 7+7 min | 1 min |
| 11 | 0 | 2 °C/s | 545 °C | 5+5 min | 3 min |
| 12 | -++- | 0.3 °C/s | 560 °C | 7+7 min | 1 min |
| 13 | --++ | 0.3 °C/s | 530 °C | 7+7 min | 5 min |
| 14 | +--+ | 4 °C/s | 530 °C | 7+7 min | 5 min |
| 15 | 0 | 2 °C/s | 545 °C | 5+5 min | 3 min |
| 16 | +--+ | 4 °C/s | 530 °C | 7+7 min | 1 min |
| 17 | -+-- | 0.3 °C/s | 560 °C | 3+3 min | 1 min |
| 18 | +--+ | 4 °C/s | 530 °C | 3+3 min | 5 min |
| 19 | 0 | 2 °C/s | 545 °C | 5+5 min | 3 min |
| 20 | +++- | 4 °C/s | 560 °C | 7+7 min | 1 min |
| 21 | ++++ | 4 °C/s | 560 °C | 7+7 min | 5 min |
| 22 | -+-+ | 0.3 °C/s | 560 °C | 3+3 min | 5 min |
| 23 | 0 | 2 °C/s | 545 °C | 5+5 min | 3 min |

3.1.5 Results and discussion

Table 3 presents the statistical significance of the FFD parameters and their interactions. The parameters and interactions were considered statistically significant when the LogWorth exceeded 2, which corresponds to a P-value lower than 0.01. Based on this criteria, only three of the four investigated parameters showed a significant influence on the solar cell performance. These three parameters of influence were the ramping speed, total anneal time and the anneal temperature. Additionally, none of the interactions between the parameters were found to be statistically significant.

Table 3: Statistical significance of parameters FFD

| Source | LogWorth | | P-value |
|--|----------|---|---------|
| Ramping speed (0.3,4) | 4.898 |  | 0.00001 |
| Total anneal time (3+3,7+7) | 2.076 |  | 0.00840 |
| Anneal temperature (530,560) | 2.027 |  | 0.00940 |
| Ramping speed * Anneal temperature | 1.354 |  | 0.04425 |
| Anneal temperature * Total anneal time | 1.350 |  | 0.04463 |
| Total anneal time * Post-anneal time | 1.332 |  | 0.04659 |
| Ramping speed * Total anneal time | 1.092 |  | 0.08088 |
| Post-anneal time (1,5) | 1.068 |  | 0.08555 |
| Anneal temperature * Post-anneal time | 0.761 |  | 0.17327 |
| Ramping speed * Post-anneal time | 0.467 |  | 0.34125 |

The influence of the process parameters on the performance was discussed, starting with the most important output parameter, namely the efficiency. Figure 16 presents the actual by predicted plot for the efficiency of the solar cells. The red line represented the ideal fit, where the predicted values matched the actual measured values. The black points corresponded to the measured efficiencies from the FFD, while the red points represented the efficiencies from the baseline measurements. The scattered distribution of the points, without a clear alignment along the ideal fit, suggested a weak link between predicted and actual values. This means that the input parameters did not have a significant influence on the efficiency.

This observation was statistically supported by the P-value of 0.6910, indicating that the model was not statistically significant and that the process parameters did not have a meaningful influence on the efficiency. The horizontal blue line in Figure 16 represents the predicted efficiency under optimal process conditions, resulting in an efficiency of 8.27%. This result was substantially lower than the target efficiency of 15% and the best-performing solar cell in the world, with an efficiency of 23.6% [3].

As expected, when only the efficiency was considered in the statistical analysis, none of the process parameters were found to have a statistically significant effect on the efficiency. When the settings for an optimal efficiency were used in the software, it predicted an efficiency of 9.77%. In Table 4 are the process settings for the optimal efficiency given.

Table 4: Settings for optimal efficiency

| Ramping speed | Anneal temperature | Total anneal time | Post-anneal time |
|---------------|--------------------|-------------------|------------------|
| 0.3 °C/s | 560 °C | 3+3 min | 1 min |

In Appendix B the individual influence of the four process parameters on the output parameters is presented. For the efficiency, the ramping speed had the most impact. A lower ramping speed was associated with higher efficiencies. Regarding anneal temperature, a lower temperature appeared to slightly improve efficiency. Moreover, a shorter anneal and post-anneal time contributed to better efficiency outcomes.

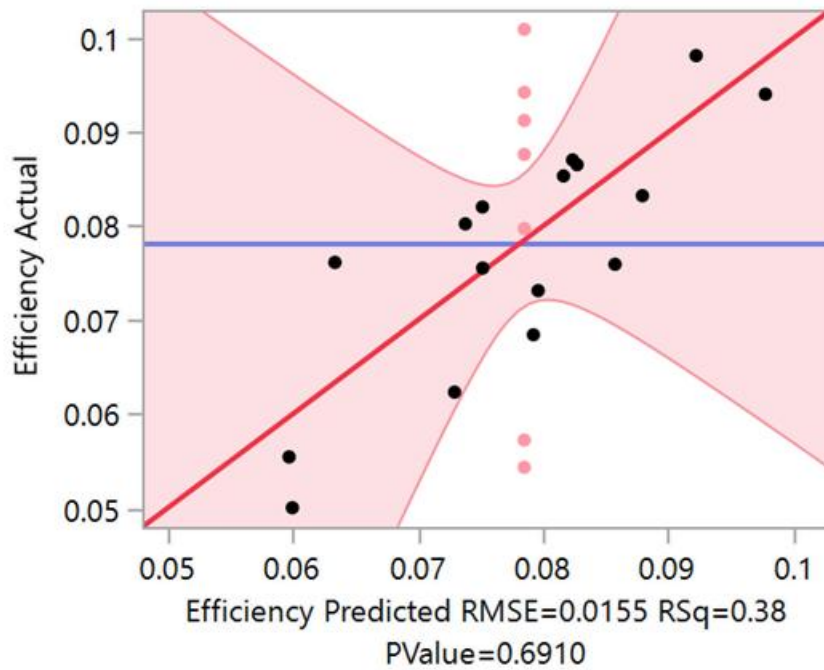


Figure 16: Actual by predicted plot for efficiency

The colors, lines and data points have consistent meanings across all plots. In the plot for lifetime shown in Figure 17, the statistical model was not significant, indicated by a P-value of 0.6305. This suggested that the process parameters did not have a meaningful influence on the lifetime. Based on the model, the predicted lifetime under optimal process conditions was 18 ns, which was substantially lower than the preferred lifetime of approximately 60 ns.

Similarly, when considering lifetime as the only response variable, none of the process parameters exhibited a statistically significant influence. Using the optimal settings for maximizing lifetime, the model predicted a value of 22 ns. Table 5 presents the process settings for obtaining the best lifetime.

Table 5: Optimal settings for lifetime

| Ramping speed | Anneal temperature | Total anneal time | Post-anneal time |
|----------------------|---------------------------|--------------------------|-------------------------|
| 4 °C/s | 560 °C | 7+7 min | 5 min |

As shown in Appendix B, the individual effects of the process parameters on lifetime revealed that increasing the ramping speed, anneal temperature and anneal time led to an increase in lifetime. In contrast, a higher post-anneal time resulted in a slightly decrease in lifetime.

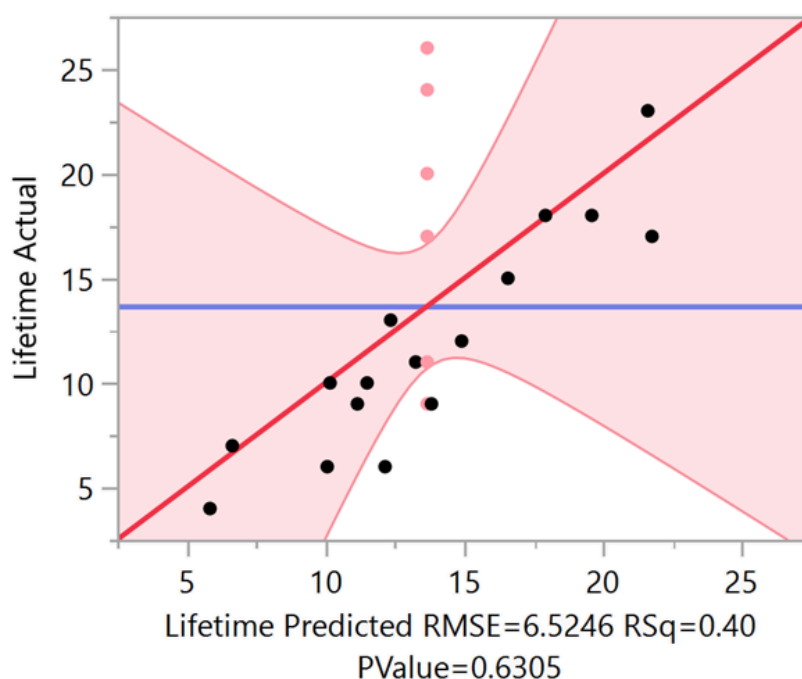


Figure 17: Actual by predicted plot for lifetime

Figure 18 illustrates the plot for the peak wavelength. The statistical analysis indicated that the model was significant, with a P-value of 0.0026, confirming that the peak wavelength was influenced by process parameter(s). The measured peak wavelengths fell within the predicted range, supporting the validity of the model. In optimal conditions, the peak wavelength was predicted to be 1145 nm. However, this value was on the lower end, as the target was to achieve a peak wavelength of 1180 nm.

A separate analysis was also performed with peak wavelength as the sole response variable. In this case, ramping speed was the only parameter that showed a statistically significant influence. Under optimal conditions, the predicted peak wavelength was 1184 nm. The settings for this condition is shown in Table 6.

Table 6: Optimal settings for peak wavelength

| Ramping speed | Anneal temperature | Total anneal time | Post-anneal time |
|---------------|--------------------|-------------------|------------------|
| 2.15 °C/s | 545 °C | 5+5 min | 3 min |

Appendix B reveals that ramping speed had a strong influence on the peak wavelength. A faster ramp speed was associated with a higher peak wavelength. On the other hand, higher values of the anneal temperature, anneal time and post-anneal time shifted the peak wavelength to lower values.

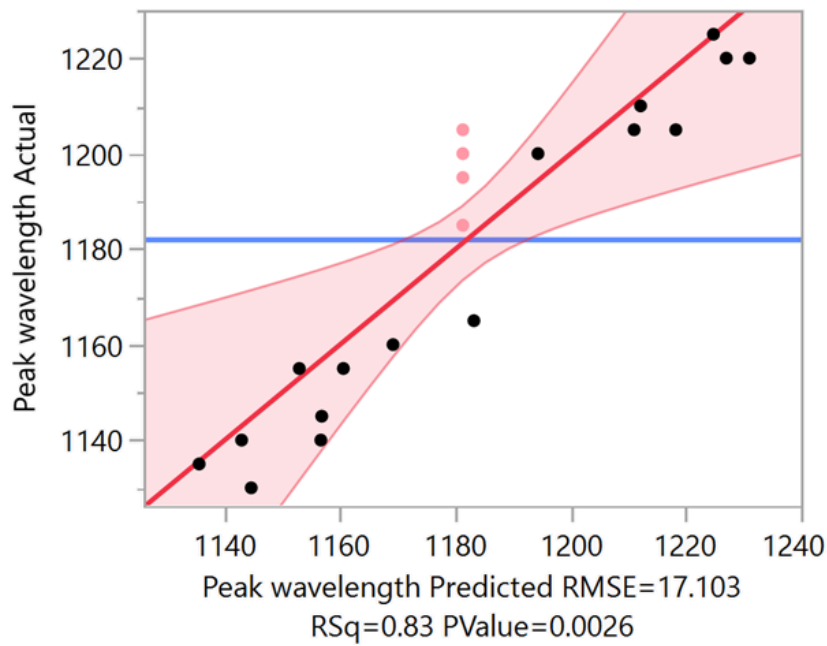


Figure 18: Actual by predicted plot for peak wavelength

In Figure 19, it was observed that the model for V_{oc} did not show strong statistical significance. However, it approached the threshold for significance with a P-value of 0.0342, indicating a weak but potentially meaningful influence of process parameter(s). Based on the model, the predicted V_{oc} under optimal conditions was 558 mV.

Shown in Appendix B, the ramping speed was the only parameter with a notable impact on the V_{oc} . Specifically, lower ramping speed corresponded to higher V_{oc} values. The other parameters exhibited only limited influence on the predicted V_{oc} .

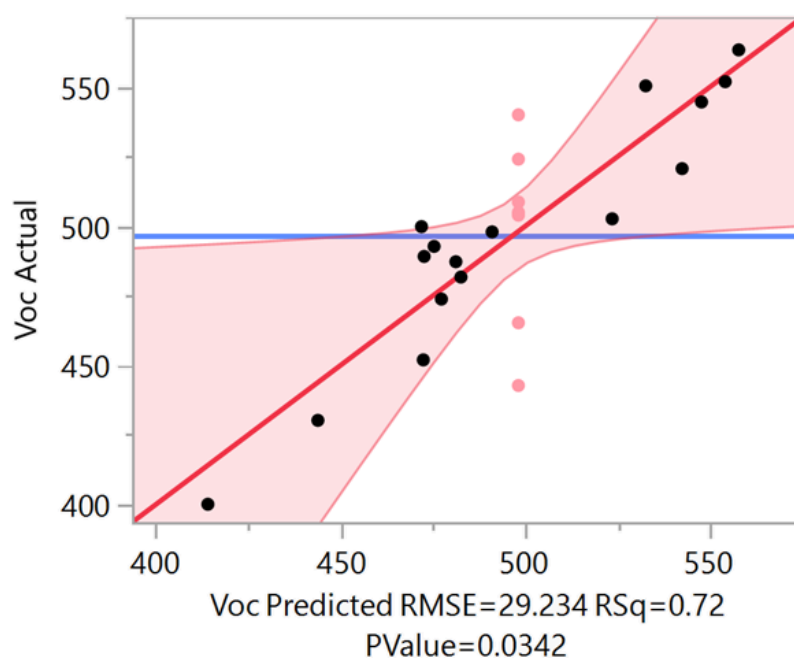


Figure 19: Actual by predicted plot for Voc

Another statistically significant model outcome was the J_{sc} , as presented in Figure 20. With a P-value slightly below 0.01, the model was considered marginally statistically significant. Based on the model prediction, the optimal J_{sc} for the overall performance was 29 mA/cm². Both V_{oc} and J_{sc} should be as high as possible to maximize the output power of the solar cell.

According to Appendix B, the ramping speed had the least influence on the J_{sc} . In fact, a lower ramping speed was associated with the lowest J_{sc} values. The remaining parameters had similar levels of influence. In general, lower values of these parameters resulted in higher J_{sc} values, suggesting that reduced thermal exposure positively affected the J_{sc} .

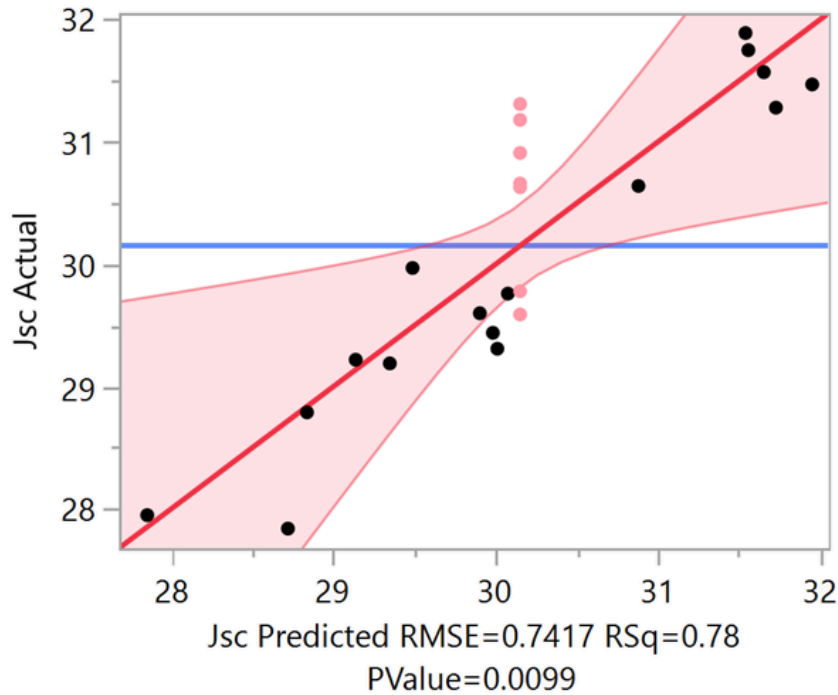


Figure 20: Actual by predicted plot for J_{sc}

The final plot, shown in Figure 21, represented the model for the FF. This model was not statistically significant, indicating that the process parameters did not have a meaningful influence on the FF. Nevertheless, the model predicted a FF of 51% for optimal performance of the solar cell. This outcome is low compared to top-performing cells, which achieve FFs of 80% [3].

Appendix B showed that ramping speed and anneal time had the greatest influence on the FF. For both parameters, lower values corresponded with higher FF outcomes. A similar trend was observed for annealing temperature, although the effect was less pronounced. In contrast, post-anneal time had virtually no influence on the FF.

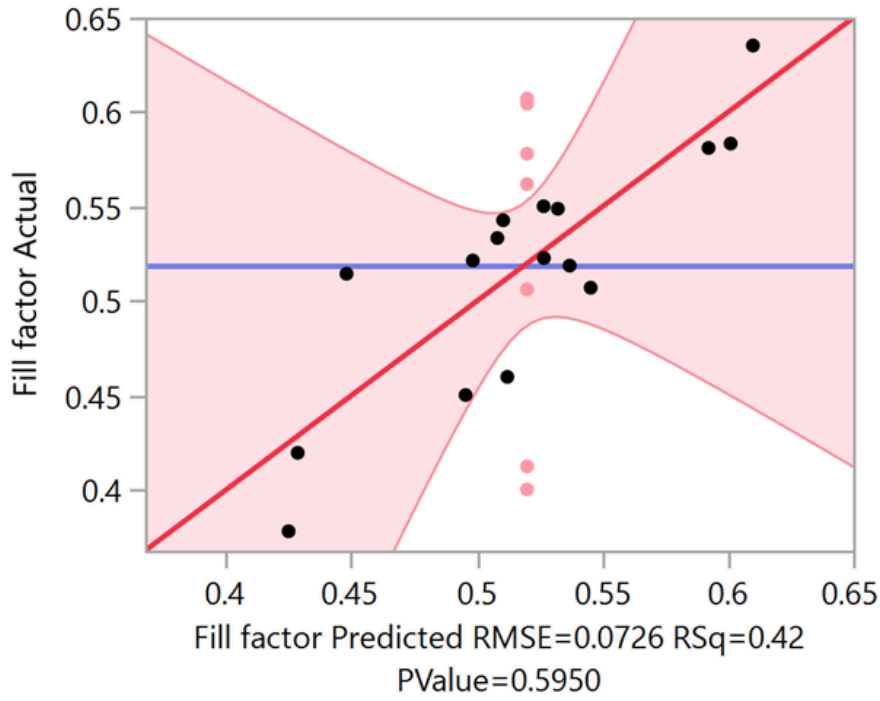


Figure 21: Actual by predicted plot for FF

The various model plots for the ratios are presented in Appendix C. Four different ratios were analyzed using the statistical software: the $\frac{Cu}{Ga+In}$ (CGI), $\frac{Ga}{Ga+In}$ (GGI), $\frac{S}{S+Se}$ (SSS) and $\frac{S+Se}{Cu+In+Ga}$ (VI/I+III). None of the models for these ratios were found to be statistically significant, indicating limited influence of process parameters on the compositions.

For the CGI ratio, the anneal time had the most noticeable impact. Where longer anneal time was associated with higher CGI values. The predicted CGI value based on the model for the optimal overall performance of the cell was 1.02.

In the case of the GGI ratio, all 4 parameters showed some level of influence. Specifically, lower ramping speed and shorter post-anneal time led to decreased GGI values, while lower anneal temperature and shorter anneal time resulted in higher GGI values. The predicted GGI value was 0.001.

Regarding the SSS ratio, ramping speed had the most effect. Lower ramping speed resulted in higher SSS values. While anneal temperature and anneal time showed no influence, longer post-anneal time led to a slightly higher SSS. The model predicted a SSS value 0.44.

Finally, the VI/I+III ratio was only slightly influenced by ramping speed, with higher values at lower ramping speeds. The other parameters had no influence on this ratio. The predicted value for VI/I+III ratio was 1.05.

Based on the overall performance of the solar cells, a model was created using JMP 6 to optimize all output characteristics, treating each output variable as equally important. From this, a new baseline set of process parameters was determined, as shown in Table 7.

Table 7: New baseline configuration

| Ramping speed | Anneal temperature | Total anneal time | Post-anneal time |
|---------------|--------------------|-------------------|------------------|
| 0.3 °C/s | 560 °C | 7+7 min | 1 min |

The predicted output variables based on the new baseline are summarized in Table 8. These values corresponded to the predictions discussed in the previous sections, representing the expected performance of the solar cell under optimized process conditions.

Table 8: Predicted output variables based on the new baseline recipe

| Output variable | Predicted value |
|-------------------------------------|-----------------------|
| Efficiency | 8.26% |
| Lifetime | 18 ns |
| Peak wavelength | 1145 nm |
| Open-circuit voltage (Voc) | 558 mV |
| Short-circuit current density (Jsc) | 29 mA/cm ² |
| Fill factor (FF) | 51% |
| CGI | 1.02 |
| GGI | 0.001 |
| SSS | 0.44 |
| VI/I+III | 1.05 |

3.2 Silver alloyed absorber layer

In addition to the FFD, a small-scale side experiment was conducted to achieve a higher efficiency. The same solar cell fabrication as described in Full factorial design of experiments was used, with one key difference. This key difference was that before the selenization process a 10 nm thick Silver (Ag) layer was evaporated onto the layer stack. This modification was implemented because the best-performing CIGS solar cell produced also contained Ag, with a $\frac{Ag}{Ag+Cu}$ (AAC) ratio of 0.19 [3].

All other fabrication and characterization steps were identical to the ones used in the FFD. For this experiment, the original baseline process parameters were used, illustrated in Table 9. This small-scale experiment was conducted on two samples.

Table 9: Old baseline for selenization process

| Ramping speed | Anneal temperature | Total anneal time | Post-anneal time |
|---------------|--------------------|-------------------|------------------|
| 2 °C/s | 550 °C | 5+5 min | 3 min |

3.2.1 Results and discussion

The results of the side experiment are summarized in Table 10. Overall, the cell performance was significantly lower compared to the original baseline without Ag. The samples exhibited a high concentration of Ag, Ga and S in the layer stack. Although these concentrations were to excessive, they reflected the intended strategy of modifying the absorber composition to improve the overall performance. This modification led to a significant increase in Ga integration, resulting in a band gap exceeding 1.3 eV, while the optimal bandgap is around 1.15 eV.

Table 10: Results samples alloyed with Ag

| Output | Sample PV24-27-4a | Sample PV24-27-4b |
|-------------------------------------|--------------------------|--------------------------|
| Efficiency | 3.24% | 2.57% |
| Lifetime | 7 ns | 5 ns |
| Peak wavelength | 990 nm | 995 nm |
| Open-circuit voltage (Voc) | 545.0 mV | 517.3 mV |
| Short-circuit current density (Jsc) | 14.62 mA/cm ² | 13.32 mA/cm ² |
| Fill factor (FF) | 38.20% | 25.68% |
| CGI | 0.97 | 0.94 |
| GGI | 0.02 | 0.05 |
| SSS | 0.21 | 0.15 |
| VI/I+III | 1.02 | 1.05 |
| AAC | 0.06 | 0.05 |

3.3 Zinc oxysulfide buffer layer

The second side experiment focused on replacing the conventional CdS buffer layer with a Zn(O,S) buffer layer, because of the toxicity concerns associated with Cd. The samples were processed following the same methodology as the Full factorial design of experiments, using the original baseline parameters outlined in Table 9. The only change was the substitution of the buffer layer with Zn(O,S), which was applied to four samples using a standardized deposition recipe. Initially, two samples were fabricated to evaluate the overall cell performance. Subsequently, two additional samples were processed, with one taken out of the Annealsys furnace at 100 °C and the other at 25 °C. This was done to assess whether the cooling temperature prior to buffer layer deposition influenced the final cell performance.

3.3.1 Results and discussion

The results of all four Zn(O,S) buffer layer samples are summarized in Table 11. The performance of the four samples was highly consistent, indicating that the applied deposition recipe was reproducible. However, the overall cell performance was significantly lower compared to cells fabricated with a CdS buffer layer. The efficiency was about half of similarly made cells with CdS. Due to this significant performance gap, which would require substantial optimization, the primary focus of this thesis remained on the FFD.

Table 11: Results samples with Zn(O,S) buffer layer

| Output | Sample PV24-27-8b | Sample PV24-27-9a | Sample PV24-27-10a (out at 25 °C) | Sample PV24-27-10b (out at 100 °C) |
|-------------------------------|------------------------------|------------------------------|--|---|
| Efficiency | 5.10% | 5.28% | 5.04% | 5.36% |
| Lifetime | 14 ns | 14 ns | 18 ns | 12 ns |
| Peak wavelength | 1185 nm | 1190 nm | 1180 nm | 1190 nm |
| Open-circuit voltage | 449.1 mV | 442.7 mV | 455.1 mV | 451.9 mV |
| Short-circuit current density | 29.73 mA/cm ² | 30.77 mA/cm ² | 27.99 mA/cm ² | 29.84 mA/cm ² |
| Fill factor | 38.20% | 38.81% | 39.58% | 39.78 |

4 Conclusion

In this final chapter, the conclusion of the experiment is presented. The main findings and suggestions for future research are discussed here.

4.1 Full factorial design

The main objective of this thesis was to increase the efficiency of the solar cells to 15%. Although this target was not achieved, the experiment proved to be valuable. It provides insight into how the output variables change in relation to the different process parameters.

The results showed that only three of the four process parameters, identified as significant in previous research, were actually significant in this experiment. These are the ramping speed, anneal temperature and anneal time. The post-anneal time had no significant impact on the overall cell performance.

Among the output variables, only the peak wavelength and J_{sc} were significantly influenced by the process parameters. The peak wavelength was clearly influenced by the ramping speed. A higher ramping speed resulted in higher peak wavelengths. The J_{sc} was mainly affected by the anneal temperature, anneal time and post-anneal time. Higher J_{sc} values were associated with lower values of these parameters.

Using this software, a new baseline for the selenization process was established. The values for the process parameters of this baseline are provided in Table 7.

These findings suggest that further optimization should focus on the metal sputtering step preceding the selenization process. This is necessary in the optimization process, because optimal selenization settings alone are insufficient to achieve world-record CIGS cell performance.

4.2 Small-scale side experiments

Despite the low efficiencies generated with Ag alloyed absorber layers, the elevated band gap suggests a potential direction for future optimization, particularly in tuning the Ga gradient across the absorber layer.

For the Zn(O,S) buffer layer, the current deposition recipe produced stable and consistent cell performance. While this is a positive outcome, the efficiencies achieved with this buffer layer were only the half of those obtained using a CdS buffer layer. This indicates that the Zn(O,S) deposition process requires further optimization. To better understand the influence of deposition parameters on cell performance, a one-factor-at-a-time experimental approach is recommended. Table 12 presents a proposed set of parameters and corresponding values for a one-factor-at-a-time experimental design.

Table 12: Parameter settings of one-factor-at-a-time experiment for a Zn(O,S) buffer layer

| Parameter | Unit | - | 0 | + |
|---------------------------------------|-------------|----------|----------|--------------|
| Power deposition 1 | W | 40 | 51 | / |
| Pressure deposition 1 | mbar | 2 | 4 | 8 |
| O ₂ /Ar ratio deposition 1 | / | / | 0 | / |
| Time deposition 1 | s | 900 | 1800 | 3600 |
| Power deposition 2 | W | / | 51 | 70 |
| Pressure deposition 2 | mbar | 2 | 4 | 8 |
| O ₂ /Ar ratio deposition 2 | / | / | 1/35 | 2/35 or 4/35 |
| Time deposition 2 | s | 900 | 1800 | 2400 or 3600 |

References

- [1] European Parliament, “Renewable energy: setting ambitious targets for Europe.” Accessed: Oct. 10, 2024. [Online]. Available: <https://www.europarl.europa.eu/topics/en/article/20171124STO88813/renewable-energy-setting-ambitious-targets-for-europe>
- [2] Solar Magazine, “What Are CIGS Thin-Film Solar Panels? When to Use Them?” Accessed: Oct. 11, 2024. [Online]. Available: <https://solarmagazine.com/solar-panels/cigs-thin-film-solar-panels/>
- [3] J. Keller *et al.*, “High-concentration silver alloying and steep back-contact gallium grading enabling copper indium gallium selenide solar cell with 23.6% efficiency,” *Nat Energy*, vol. 9, no. 4, 2024, doi: 10.1038/s41560-024-01472-3.
- [4] “🗨️ 1 - Annealsys introduces pulse annealing.” Accessed: Apr. 25, 2025. [Online]. Available: <https://www.annealsys.com/news/news/2022/annealsys-introduces-pulse-annealing-hu50902.html>
- [5] “Scanning Electron Microscopes (SEM) | Science Basics | Products | JEOL Ltd.” Accessed: Apr. 25, 2025. [Online]. Available: <https://www.jeol.com/products/science/sem.php>
- [6] “Full Factorial Design: A Comprehensive Guide.” Accessed: May 27, 2025. [Online]. Available: <https://datatab.net/tutorial/full-factorial-design>
- [7] B. Salhi, “The Photovoltaic Cell Based on CIGS: Principles and Technologies,” 2022. doi: 10.3390/ma15051908.
- [8] K. H. Ong *et al.*, “Review on substrate and molybdenum back contact in CIGS thin film solar cell,” 2018. doi: 10.1155/2018/9106269.
- [9] S. Mandati, P. Misra, B. V. Sarada, and T. N. Rao, “Copper Chalcopyrites for Solar Energy Applications,” 2019. doi: 10.1007/s12666-018-1455-0.
- [10] A. Kakade, K. B. Chavan, S. Chaure, and N. B. Chaure, “The role of window layers on the simulated performance of CIGS solar cell characteristics using SCAPS-1D,” *Next Research*, vol. 2, no. 2, p. 100334, Jun. 2025, doi: 10.1016/J.NEXRES.2025.100334.
- [11] U. P. Singh and S. P. Patra, “Progress in polycrystalline thin-film Cu(In,Ga)Se₂ solar cells,” 2010. doi: 10.1155/2010/468147.
- [12] S. Niki *et al.*, “CIGS absorbers and processes,” *Progress in Photovoltaics: Research and Applications*, vol. 18, no. 6, 2010, doi: 10.1002/pip.969.
- [13] C. H. Huang, W. J. Chuang, C. P. Lin, Y. L. Jan, and Y. C. Shih, “Deposition technologies of high-efficiency cigs solar cells: Development of two-step and co-evaporation processes,” *Crystals (Basel)*, vol. 8, no. 7, 2018, doi: 10.3390/cryst8070296.
- [14] H. P. Kuo, H. A. Tsai, A. N. Huang, and W. C. Pan, “CIGS absorber preparation by non-vacuum particle-based screen printing and RTA densification,” *Appl Energy*, vol. 164, 2016, doi: 10.1016/j.apenergy.2015.04.002.
- [15] S. Suresh and A. R. Uhl, “Present Status of Solution-Processing Routes for Cu(In,Ga)(S,Se)₂ Solar Cell Absorbers,” 2021. doi: 10.1002/aenm.202003743.

- [16] S. Mandati and B. V. Sarada, "Electrodeposited chalcopyrite CuInGaSe_2 absorbers for solar energy harvesting," *Mater Sci Energy Technol*, vol. 3, 2020, doi: 10.1016/j.mset.2020.03.001.
- [17] S. Y. Kim and J. H. Kim, "Fabrication of CIGS thin films by using spray pyrolysis and post-selenization," *Journal of the Korean Physical Society*, vol. 60, no. 12, 2012, doi: 10.3938/jkps.60.2018.
- [18] T. I. Alanazi, "Current spray-coating approaches to manufacture perovskite solar cells," *Results Phys*, vol. 44, 2023, doi: 10.1016/j.rinp.2022.106144.
- [19] Jelle Van Lommel, "Optimization of thin film chalcogenide solar cell baseline process," 2024.
- [20] B. S. Yadav, S. R. Dey, and S. R. Dhage, "Inkjet printed $\text{CuIn}(1-X)\text{GaXSe}_2$ thin film by controlled selenium distribution for improved power conversion efficiency in chalcopyrite solar cells," *Applied Surface Science Advances*, vol. 6, 2021, doi: 10.1016/j.apsadv.2021.100144.
- [21] Stijn Driessen, "Development of ultra-thin CIGS absorber material with alkali treatment for solar cell production," 2021.
- [22] "AM0, AM1.5, and AM1.5G: Air Mass Standards for Solar Applications Understanding Solar Radiation Attenuation through the Atmosphere - EnliTech." Accessed: May 17, 2025. [Online]. Available: <https://enlitechnology.com/blog/measuring-atmospheric-mass-am0-am1-5-and-am1-5g-attenuation-of-sunlight-through-the-atmosphere/>

| Ramping Speed °C/sec | Anneal temperature °C | Anneal time Min. | Post-anneal time Min. | Sample name | EDS (energy dispersive spectroscopy) | | | | | | | | | | | | (TR)PL | | I-V | | | |
|-------------------------|--------------------------|---------------------|--------------------------|-------------|--------------------------------------|------|-------|-------|------|-------|-------|------------|------------|----------|-------------------|--------------------|---------------|----|---------------------------|----------|--------|----------------|
| | | | | | GaI | CGI | S | Cu | Ga | Se | In | Cu/(In+Ga) | Ga/(In+Ga) | S/(S+Se) | (S+Se)/(Cu+In+Ga) | Peak position (nm) | Lifetime (ns) | t1 | Jsc [mA/cm ²] | Voc [mV] | FF [%] | Efficiency [%] |
| 2 | 545 | 5 | 3 | PV24-27-11b | 0.04 | 0.87 | 17.81 | 22.56 | 1.10 | 33.55 | 24.98 | 0.87 | 0.04 | 0.35 | 1.06 | 1195 | 20 | | 29.59 | 524.0 | 60.73% | 9.42% |
| 4 | 560 | 3 | 1 | PV24-27-12a | 0.03 | 0.84 | 14.32 | 22.95 | 0.89 | 35.38 | 26.46 | 0.84 | 0.03 | 0.29 | 0.99 | 1220 | 11 | | 31.57 | 489.1 | 63.54% | 9.81% |
| 4 | 530 | 3 | 1 | PV24-27-12b | 0.00 | 0.85 | 12.36 | 22.59 | 0.12 | 38.46 | 26.47 | 0.85 | 0.00 | 0.24 | 1.03 | 1220 | 4 | | 31.28 | 400.2 | 58.35% | 7.31% |
| 2 | 545 | 5 | 3 | PV24-27-13a | 0.02 | 0.90 | 17.80 | 22.83 | 0.43 | 34.09 | 24.85 | 0.90 | 0.02 | 0.34 | 1.08 | 1200 | 26 | | 30.91 | 539.9 | 60.46% | 10.09% |
| 0.3 | 530 | 3 | 5 | PV24-27-13b | 0.03 | 0.95 | 23.06 | 24.16 | 0.64 | 27.36 | 24.78 | 0.95 | 0.03 | 0.46 | 1.02 | 1140 | 10 | | 29.60 | 499.8 | 51.46% | 7.61% |
| 0.3 | 530 | 3 | 1 | PV24-27-14a | 0.01 | 0.87 | 22.90 | 22.99 | 0.36 | 27.61 | 26.14 | 0.87 | 0.01 | 0.45 | 1.02 | 1155 | 7 | | 29.97 | 481.7 | 52.29% | 7.55% |
| 2 | 545 | 5 | 3 | PV24-27-14b | 0.01 | 0.83 | 19.90 | 21.99 | 0.32 | 31.62 | 26.17 | 0.83 | 0.01 | 0.39 | 1.06 | 1200 | 24 | | 29.78 | 465.3 | 41.26% | 5.72% |
| 4 | 560 | 3 | 5 | PV24-27-15a | 0.04 | 0.93 | 16.59 | 24.23 | 1.00 | 33.25 | 24.93 | 0.93 | 0.04 | 0.33 | 0.99 | 1205 | 23 | | 31.75 | 497.9 | 55.03% | 8.70% |
| 0.3 | 560 | 7 | 5 | PV24-27-15b | 0.01 | 0.91 | 29.37 | 23.42 | 0.34 | 21.41 | 25.46 | 0.91 | 0.01 | 0.58 | 1.03 | 1135 | 15 | | 27.95 | 550.3 | 52.16% | 8.02% |
| 0.3 | 530 | 7 | 1 | PV24-27-16a | 0.02 | 0.92 | 22.46 | 23.21 | 0.53 | 29.15 | 24.65 | 0.92 | 0.02 | 0.44 | 1.07 | 1155 | 9 | | 29.44 | 544.5 | 51.89% | 8.32% |
| 2 | 545 | 5 | 3 | PV24-27-16b | 0.03 | 0.94 | 14.91 | 23.92 | 0.65 | 35.75 | 24.77 | 0.94 | 0.03 | 0.29 | 1.03 | 1200 | 20 | | 31.18 | 504.9 | 50.63% | 7.97% |
| 0.3 | 560 | 7 | 1 | PV24-27-17a | 0.01 | 1.02 | 24.84 | 24.91 | 0.17 | 25.77 | 24.31 | 1.02 | 0.01 | 0.49 | 1.02 | 1130 | 18 | | 28.79 | 563.2 | 53.35% | 8.55% |
| 0.3 | 530 | 7 | 5 | PV24-27-17b | 0.02 | 0.93 | 19.72 | 23.48 | 0.59 | 31.50 | 24.72 | 0.93 | 0.02 | 0.39 | 1.05 | 1160 | 9 | | 29.76 | 502.6 | 50.72% | 7.59% |
| 4 | 530 | 7 | 5 | PV24-27-18a | 0.03 | 0.67 | 23.80 | 18.93 | 0.88 | 29.16 | 27.22 | 0.67 | 0.03 | 0.45 | 1.13 | 1225 | 13 | | 31.89 | 487.2 | 54.90% | 8.53% |
| 2 | 545 | 5 | 3 | PV24-27-18b | 0.00 | 0.90 | 15.69 | 22.64 | 0.05 | 36.40 | 25.22 | 0.90 | 0.00 | 0.30 | 1.09 | 1205 | 11 | | 31.31 | 503.9 | 57.81% | 9.12% |
| 4 | 530 | 7 | 1 | PV24-27-19a | 0.01 | 0.91 | 11.34 | 23.39 | 0.38 | 39.68 | 25.21 | 0.91 | 0.01 | 0.22 | 1.04 | 1205 | 10 | | 30.64 | 492.7 | 54.29% | 8.20% |
| 0.3 | 560 | 3 | 1 | PV24-27-19b | 0.01 | 0.95 | 21.12 | 23.87 | 0.27 | 29.96 | 24.77 | 0.95 | 0.01 | 0.41 | 1.04 | 1145 | 6 | | 29.31 | 551.8 | 58.12% | 9.40% |
| 4 | 530 | 3 | 5 | PV24-27-20a | 0.00 | 0.99 | 9.40 | 24.26 | 0.10 | 41.91 | 24.33 | 0.99 | 0.00 | 0.18 | 1.05 | 1210 | 6 | | 31.47 | 490.3 | 46.00% | 6.23% |
| 2 | 545 | 5 | 3 | PV24-27-20b | 0.00 | 0.91 | 13.95 | 23.19 | 0.00 | 37.28 | 25.59 | 0.91 | 0.00 | 0.27 | 1.05 | 1195 | 9 | | 30.66 | 508.6 | 56.20% | 8.76% |
| 4 | 560 | 7 | 1 | PV24-27-21a | 0.02 | 0.94 | 13.29 | 22.97 | 0.39 | 39.24 | 24.10 | 0.94 | 0.02 | 0.25 | 1.11 | 1200 | 18 | | 29.22 | 452.0 | 37.83% | 5.00% |
| 0.3 | 560 | 3 | 5 | PV24-27-21b | 0.05 | 0.98 | 19.43 | 24.29 | 1.19 | 31.55 | 23.53 | 0.98 | 0.05 | 0.42 | 1.04 | 1165 | 17 | | 27.84 | 473.8 | 54.54% | 7.48% |
| 2 | 545 | 5 | 3 | PV24-27-22a | 0.03 | 0.92 | 22.19 | 22.83 | 0.68 | 30.21 | 24.09 | 0.92 | 0.03 | 0.42 | 1.10 | 1140 | 12 | | 29.19 | 520.6 | 45.04% | 6.84% |
| 0.3 | 560 | 3 | 3 | PV24-27-22b | 0.01 | 0.91 | 15.78 | 23.13 | 0.22 | 35.76 | 25.11 | 0.91 | 0.01 | 0.31 | 1.06 | 1185 | 17 | | 30.63 | 442.8 | 40.04% | 5.43% |

Appendix B

